



# Interstellar Pickup Ion Observations to 60 au

D. J. McComas<sup>1</sup> , B. L. Shrestha<sup>1</sup> , G. Livadiotis<sup>1</sup> , J. R. Szalay<sup>1</sup> , E. J. Zirnstein<sup>1</sup> , H. A. Elliott<sup>2</sup> , P. C. Brandt<sup>3</sup> ,  
A. R. Poppe<sup>4</sup> , K. N. Singer<sup>5</sup> , A. Stern<sup>5</sup> , and A. Verbiscer<sup>6</sup> ,  
the New Horizons Heliophysics Team

<sup>1</sup>Department of Astrophysical Sciences, Princeton University, Princeton, NJ 08544, USA; [dmccomas@princeton.edu](mailto:dmccomas@princeton.edu)

<sup>2</sup>Southwest Research Institute, San Antonio, TX 78228, USA

<sup>3</sup>The Johns Hopkins University Applied Physics Laboratory, Laurel, MD 20723, USA

<sup>4</sup>Space Sciences Laboratory, University of California at Berkeley, Berkeley, CA 94720, USA

<sup>5</sup>Southwest Research Institute, Boulder, CO 80302, USA

<sup>6</sup>Department of Astronomy, University of Virginia, Charlottesville, VA 22904, USA

Received 2024 November 27; revised 2025 January 2; accepted 2025 January 4; published 2025 February 10

## Abstract

Prior to the Solar Wind Around Pluto (SWAP) observations from New Horizons, the only significant interstellar pickup ion (PUI) observations were taken inside 5.4 au from the Ulysses and 1 au missions. Here, we analyze SWAP data to provide the first comprehensive radial profile of interstellar PUIs in the outer heliosphere from  $\sim 22$  to 60 au. This study is the first to combine the low time resolution (one day) data inside 49.5 au with the high time resolution (half hour) data outside of that. We show that these two data sets can be reliably analyzed together in what is now a nearly continuous set of PUI observations. We derive radial gradients for all of the PUI parameters, as well as ratios to their solar wind counterparts from these combined data and extrapolate them out to a nominal termination shock distance at  $\sim 90$  au. We find that the fraction of PUIs to all ions in the solar wind continues to grow, reaching  $\sim 18\%$  by 60 au and extrapolated to be  $\sim 30\%$  at 90 au. The PUI internal pressure is  $\sim 11\%$  of the solar wind dynamic pressure at 60 au and expected to be  $\sim 21\%$  by 90 au. Such large values further highlight the importance of PUIs as the dominant driver of the physics of the outer heliosphere, as well as at the termination shock.

*Unified Astronomy Thesaurus concepts:* Plasma physics (2089); Space plasmas (1544); Heliosphere (711); Solar wind (1534); Pickup ions (1239); Interplanetary shocks (829)

## 1. Introduction

The solar wind travels nearly radially outward in all directions from the Sun, filling the heliosphere with solar plasma and magnetic field. The magnetized plasmas of the solar wind and surrounding very local interstellar medium (VLISM) cannot interpenetrate each other, and thus a boundary—the heliopause—separates them. In contrast, the interstellar neutral atoms from the VLISM are uncharged and travel freely across the heliopause and into the heliosphere at the relative velocity between the Sun and VLISM, which is  $\sim 25 \text{ km s}^{-1}$  (e.g., D. J. McComas et al. 2015).

As the interstellar neutrals drift deeper into the heliosphere, more and more of them are ionized (for H, most are ionized through charge exchange with the solar wind protons) and become “picked up” in the solar wind flow. As pickup ions (PUIs), they gyrate in the interplanetary magnetic field (IMF) as they are carried out at the solar wind bulk speed. This combined motion means that they are observed in the solar frame to be moving at speeds from near zero (their initial neutral inflow speed) up to roughly twice the solar wind speed over different portions of their gyro-motion. This motion produces “ring-like” distributions in velocity space, which quickly scatter in angle, forming nearly isotropic shell distributions. These shells then slowly cool to lower energies in the solar wind frame and evolve closer to the solar wind speed over time. As this happens, new

PUIs are being produced and continuously populating the outermost shell of the PUI distribution.

E. Möbius et al. (1985) made the first in situ measurements of interstellar PUIs ( $\text{He}^+$ ) from a spacecraft at 1 au. Many other species of PUIs were subsequently measured between  $\sim 1.4$  and 5.4 au by the Solar Wind Ion Composition Spectrometer instrument (G. Gloeckler et al. 1992) on the ESA/NASA Ulysses mission, which made measurements out of the ecliptic plane, up to  $>80^\circ$  latitudes. These included  $\text{H}^+$ ,  $\text{He}^+$ ,  $\text{N}^+$ ,  $\text{O}^+$ , and  $\text{Ne}^+$  PUIs (J. Geiss et al. 1994), as well as  $\text{He}^{++}$  and  $^3\text{He}^+$  PUIs (G. Gloeckler et al. 1997). Beyond the orbit of Jupiter, there had been almost no PUI measurements. Those limited observations included a depletion of interstellar  $\text{H}^+$  PUIs at the Cassini spacecraft between 6.4 and 8.2 au for PUI trajectories passing close to the Sun—this feature was dubbed the interstellar neutral hydrogen “shadow” by D. J. McComas et al. (2004). Other studies of Pioneer 10 and 11 data at  $\sim 8$  au (D. S. Intriligator et al. 1996) and 16 au (J. D. Mihalov & P. R. Gazis 1998) showed some “possible signatures” of interstellar  $\text{H}^+$  PUIs. For a detailed historical review of interstellar PUI measurements, see E. J. Zirnstein et al. (2022a) and references therein.

In the modern era, the Solar Wind Around Pluto (SWAP) instrument (D. J. McComas et al. 2008) on the New Horizons (NH) mission (see Space Science Reviews Volume 140, Issues 1–4, Ed. C. T. Russell, 2008) has been uniquely measuring both the tenuous solar wind and PUIs in the outer heliosphere with exceptionally high sensitivity and a very large field of view. With SWAP’s innovative design, we simultaneously measure both the core solar wind (H. A. Elliott et al. 2016, 2018, 2019) and  $\text{H}^+$  PUIs (D. J. McComas et al. 2010, 2017,

2021, 2022; B. M. Randol et al. 2012, 2013; E. J. Zirnstein et al. 2018; P. Swaczyna et al. 2019, 2020; B. L. Shrestha et al. 2024). Now, as it heads out of the solar system, SWAP has been returning detailed distributions that allow us to derive the properties of interstellar H<sup>+</sup> PUIs in the outer heliosphere for the first time.

SWAP was only powered on for brief intervals of spacecraft contact between 8 and 22 au, leading to only sporadic observations of PUIs over these heliocentric distances (D. J. McComas et al. 2010; B. M. Randol et al. 2012, 2013). Then, starting in 2012, we were allowed to keep SWAP on nearly continuously and have been producing excellent solar wind and hydrogen PUI observations ever since; these observations now span from  $\sim 22$  to 60 au. The first major analysis of the data from  $\sim 22$  to 38 au (D. J. McComas et al. 2017) showed that the PUI internal pressure was significantly greater than the core solar wind dynamic and magnetic field pressures and increasing with respect to them throughout these distances, as had been previously theorized (e.g., H. J. Fahr & H. Fichtner 1995, M. A. Lee 1999, H. J. Fahr & K. Scherer 2005). The addition of PUIs also slows the core solar wind, because the newly born PUIs need to be accelerated up to join the solar wind bulk flow. By comparing 1 au observations with SWAP core solar wind speed measurements from 30 to 43 au, H. A. Elliott et al. (2019) demonstrated a 5%–7% slowing, consistent with expectations for PUI mass loading.

This paper continues our refinement of the extraction of quantitative moment-like PUI parameters from the SWAP observations. Initially, we used the classic V. M. Vasyliunas & G. L. Siscoe (1976) model of PUI distributions, which includes ionization of the interstellar neutrals, instantaneous scattering into an isotropic distribution in the solar wind frame, convection, and adiabatic cooling. D. J. McComas et al. (2017) expressed this in the solar wind frame as

$$f(r, w) = \frac{3}{8\pi} \frac{\beta_0 r_0^2}{r u_{\text{sw}} v_b^3} w^{-3/2} n_{\text{H,TS}} \exp\left(-\frac{\lambda}{r} \frac{\theta}{\sin\theta} w^{-3/2}\right) \Theta(1-w), \quad (1)$$

where  $u_{\text{sw}}$  is the solar wind bulk speed in the solar frame,  $\beta_0$  is the ionization rate normalized to  $r_0 = 1$  au,  $n_{\text{H,TS}}$  is the density of the interstellar neutral hydrogen at the upwind termination shock,  $\theta$  is the angle between radial and the interstellar hydrogen inflow direction,  $\lambda$  is the hydrogen ionization  $e$ -folding cavity size, and  $\Theta$  is the Heaviside step function. This equation includes the local hydrogen ionization rate,  $\beta_0$ , and ionization cavity size,  $\lambda$ , which are physically meaningful parameters. However, D. J. McComas et al. (2017) found that, using this equation, the lowest reduced  $\chi^2$  differences between the model and the data generally required unphysically large or small values for one or both parameters.

The primary missing physics in Equation (1) is that it only includes simple adiabatic cooling and does not account for the possibility of additional PUI heating, which routinely arises through PUI-generated waves and turbulence and at interplanetary shocks. D. J. McComas et al. (2021) used the generalization of this equation (J. H. Chen et al. 2014; P. Swaczyna et al. 2020), which includes an arbitrary cooling index,  $\alpha$ , defined by  $(v/v_b)^\alpha = (r_{\text{pickup}}/r)$ , where  $v$  is the local PUI speed at the measurement distance,  $r$ , and  $v_b$  is the injection speed at the distance where the ion was picked up,  $r_{\text{pickup}}$ , and also allows for PUI losses through reneutralization

by charge exchange with other interstellar atoms. This leads to

$$f(r, w) = \frac{\alpha S(r, w)}{4\pi} \frac{\beta_0 r_0^2}{r u_{\text{sw}} v_b^3} w^{\alpha-3} n_{\text{H,TS}} \exp\left(-\frac{\lambda}{r} \frac{\theta}{\sin\theta} w^{-\alpha}\right) \Theta(1-w), \quad (2)$$

where  $w = v/v_b$ , and  $S(r, w)$  is the survival probability of PUIs from where they were picked up to where they are subsequently observed.

D. J. McComas et al. (2021) used Equation (2), as well as several other improvements and modifications to the analysis process, and extended the SWAP PUI data out to 46.6 au, in addition to reanalyzing the previously published (D. J. McComas et al. 2017) PUI observations inside of  $\sim 38$  au. This new procedure no longer required the hydrogen ionization cavity to be a fitting parameter, and instead we set it to 4 au (e.g., J. M. Sokoł et al. 2019). This value varies by only  $\sim 1$  au over the solar cycle (D. Rucinski & M. Bzowski 1995), which has almost no effect at much larger heliocentric distances of SWAP observations. The normalized hydrogen ionization rate, on the other hand, is far more variable, and because it is a local measure, it still needs to be a fitting parameter. The improved fitting procedure generally finds values in the physically expected range of  $\sim 2 \times 10^{-7}$  to  $\sim 2 \times 10^{-6} \text{ s}^{-1}$  (Swaczyna et al. 2020) in contrast to the earlier study.

That D. J. McComas et al. (2021) study found that the PUI cooling index revealed there was additional heating going into the PUIs ( $\alpha > 3/2$ ) for over 93% of the daily averaged samples in the range from  $\sim 22$  to 47 au. These authors examined the radial variations of the PUI parameters and their ratios to their core solar wind counterparts, as well as extrapolating these values to 90 au as a proxy for likely values ahead of the termination shock. They also examined 39 traveling interplanetary shocks using superposed epoch analysis of the 1 day resolution data available for those distances. E. J. Zirnstein et al. (2018) made a detailed study of one strong shock at  $\sim 34$  au that happened to occur nearly at one particular day sample boundary. This allowed those authors to determine that, while the total energy flux per particle was approximately conserved, the PUIs gained energy, and the core solar wind ions lost energy in the shock frame.

D. J. McComas et al. (2017) showed that some traveling interplanetary shocks generate suprathermal PUI “tails” extending above the PUI cutoff, and E. J. Zirnstein et al. (2018) showed that, for the strong shock they studied, the tail accounted for  $\sim 20\%$  of the total downstream energy flux. B. L. Shrestha et al. (2024) went on to examine five distant interplanetary shocks from 24 to 37 au in more detail. These authors used the available 1 day data and found shock compression ratios from 1.4 to 3.2. They also showed that the variation of the number density in the downstream H<sup>+</sup> PUI tails increases with stronger shocks.

On 2021 February 19 with NH at  $\sim 49.5$  au, we uploaded new flight software into SWAP that reassigned memory and telemetry usage and cut the cadence of observations from  $\sim 1$  day down to roughly half an hour (D. J. McComas et al. 2022). That study documents the changes to the flight software and analysis in detail. For the ground software, the analysis code still uses Equation (2) and minimizes the reduced  $\chi^2$  values of the differences between the forward model and SWAP data. However, with  $\sim 50$  times lower counting statistics, we needed to modify the data point selection for comparison. We did this in three areas—below the proton peak, around the PUI cutoff,

and between the solar wind proton and alpha peaks, where we were able to pick up one data point in most energy spectra. This is likely because, in addition to the solar wind being generally cold at these large distances, the observed proton and alpha peaks are narrower, owing to less solar wind variation over shorter integration times. We then again iteratively fit Equation (2) to the remaining points, minimized the reduced  $\chi^2$ , and rejected all data points where the minimized reduced  $\chi^2 > 3$  (see D. J. McComas et al. 2022 for details of how we processed the high-resolution data).

D. J. McComas et al. (2022) went on to use these new PUI data to study the first seven PUI-mediated interplanetary shocks with high time resolution data. In that study, we resolved the shock structures with gradually increasing PUI pressure and shock widths of  $\sim 0.05\text{--}0.13$  au. We also showed that the PUIs are preferentially compressed across the shocks and heated for compression ratios  $> \sim 1.5$ . In contrast, the core solar wind did not show consistent changes across the shocks, indicating that they do not participate strongly in the large-scale fluid-like interactions of the combined solar wind and PUI plasma of the outer heliosphere.

Most recently, G. Livadiotis et al. (2024) examined the cooling index  $\alpha$ , and showed that it is related to polytropic processes and the polytropic index  $\gamma$  simply by  $\alpha = \frac{1}{2} + (\gamma - 1)^{-1}$ . They further developed the connection between the cooling index and thermodynamic kappa parameter  $\kappa$ , which is the other independent thermodynamic parameter, besides temperature, that governs non-Maxwellian particle distributions, or kappa distributions. G. Livadiotis et al. (2024) were able to characterize the thermodynamic evolution of PUI distributions from their incorporation into the solar wind through their combined evolution as the solar wind moves out through the heliosphere. These authors showed that their theory did a good job of explaining the evolution of thermodynamics in terms of  $\kappa$  and  $\alpha$  (or  $\gamma$ ), seen from 1 au observations, through SWAP observations halfway to the termination shock and even out to Interstellar Boundary Explorer (IBEX) observations of Energetic Neutral Atoms (ENAs) from the heliosheath (see Figure 6 in G. Livadiotis et al. 2024). These authors recommended that “*Going forward, we suggest that studies of PUIs seeking to understand the underlying physics of these important particles rely on the thermodynamic parameter of kappa, and its association with the polytropic index, and not on an ad hoc cooling index.*”

In this study, we extend the SWAP observations of PUIs out to 60 au (59.854 au) with data through 2024 September 13. In Section 2, we examine the new PUI observations and compare the measurements made with 1 day resolution with those of the improved  $\sim 30$  minute resolution to ensure that the small differences in analysis technique do not introduce any offsets that could affect using the combined data. Section 3 extrapolates the PUI variations out to the range of termination shock distances and compares these to the earlier extrapolations of D. J. McComas et al. (2021). Finally, Section 4 summarizes these findings and discusses some of the implications of the new measurements and their extrapolations to the termination shock. This study, including references to specific aspects of the analysis that have been described previously, provides all the information needed to understand how we derive the moment-like PUI properties from SWAP, and it serves as the citable reference for the entire SWAP PUI data set from  $\sim 22$  to 60 au.

## 2. New PUI Observations

The final interval of low ( $\sim 1$  day) time resolution SWAP PUI observations from 2020 January 1 to 2021 February 18 ( $\sim 46.4\text{--}49.5$  au) has never been analyzed or published before, as these came after the end of the D. J. McComas et al. (2021) study and before the initial high ( $\sim 30$  minute) time resolution PUI study (D. J. McComas et al. 2022). Figure 1 shows those data in our “standard” format from the last two PUI observation studies. We note that these data include three additional PUI-mediated interplanetary shocks that have not been published before, on 2020 February 8, March 9, and April 6, at 46.5, 46.8, and 47.0 au, respectively. As with most other shocks observed at such large distances in the heliosphere, the PUI properties varied across the shocks in consistent and expected ways, while the core solar wind largely did not (D. J. McComas et al. 2021, 2022). These and other smaller structures occurred over a year-long interval of otherwise generally decreasing solar wind speed.

Because of the need to slightly change the analysis procedure between the low time resolution ( $\sim 1$  day) PUI parameters and the data with poorer statistics but significantly higher time resolution, as described above, we examine the data around this transition in detail. Figure 2 shows observations for one solar rotation on either side of this change. On the left side of this figure, the black dots show the onboard day-averaged data points using the same general analysis process described in D. J. McComas et al. (2021) for all earlier data. We use gray dots throughout this study to represent the high-resolution ( $\sim 30$  minute) data. These are plotted on the right side of Figure 2 using the slightly revised analysis process needed for higher temporal resolution (D. J. McComas et al. 2022). Red dots and error bars show day-averaged values derived from the high-resolution data and their standard deviations. Finally, the black dots on the right side represent high-resolution data that we summed on the ground to produce day intervals and then processed using the same (D. J. McComas et al. 2021) methodology as we did for the other day-resolution data. We note that, if others would like to use lower-time-resolution data like the 1 day cadence, they should start with the high-resolution half-hour data and statistical average them as we did for the red dots, as this method is more accurate for time-variable phenomena like the solar wind and PUIs.

The first and most obvious thing in Figure 2 is how much more detailed the observations are with  $\sim 50$  times higher time resolution (gray dots). In addition, while we see much more of the detailed solar wind and PUI structure, there is no significant discontinuity or other apparent change in the values of the solar wind or PUI parameters across this time resolution boundary. In particular, (1) the low-resolution points match well across that transition, independent of whether the day summing was done on board (black) or on the ground (red), and (2) the independently derived low- and high-resolution points on the right side of Figure 2 match reasonably well for all of the speed and both densities, temperatures, pressures, and  $\alpha$  or  $\gamma$ . While there is a small difference between the red and black dots on the right side, in most cases the black dots are covered by the red  $1\sigma$  standard deviations. However, for the PUI density and temperature, there is a more consistent offset at the  $\sim 1\sigma$  level; this is accounted for by additional points in the improved fitting of the high time resolution data.

Finally, the reduced  $\chi^2$  values in Figure 2 are not expected to be the same, since two completely different fits were used for the



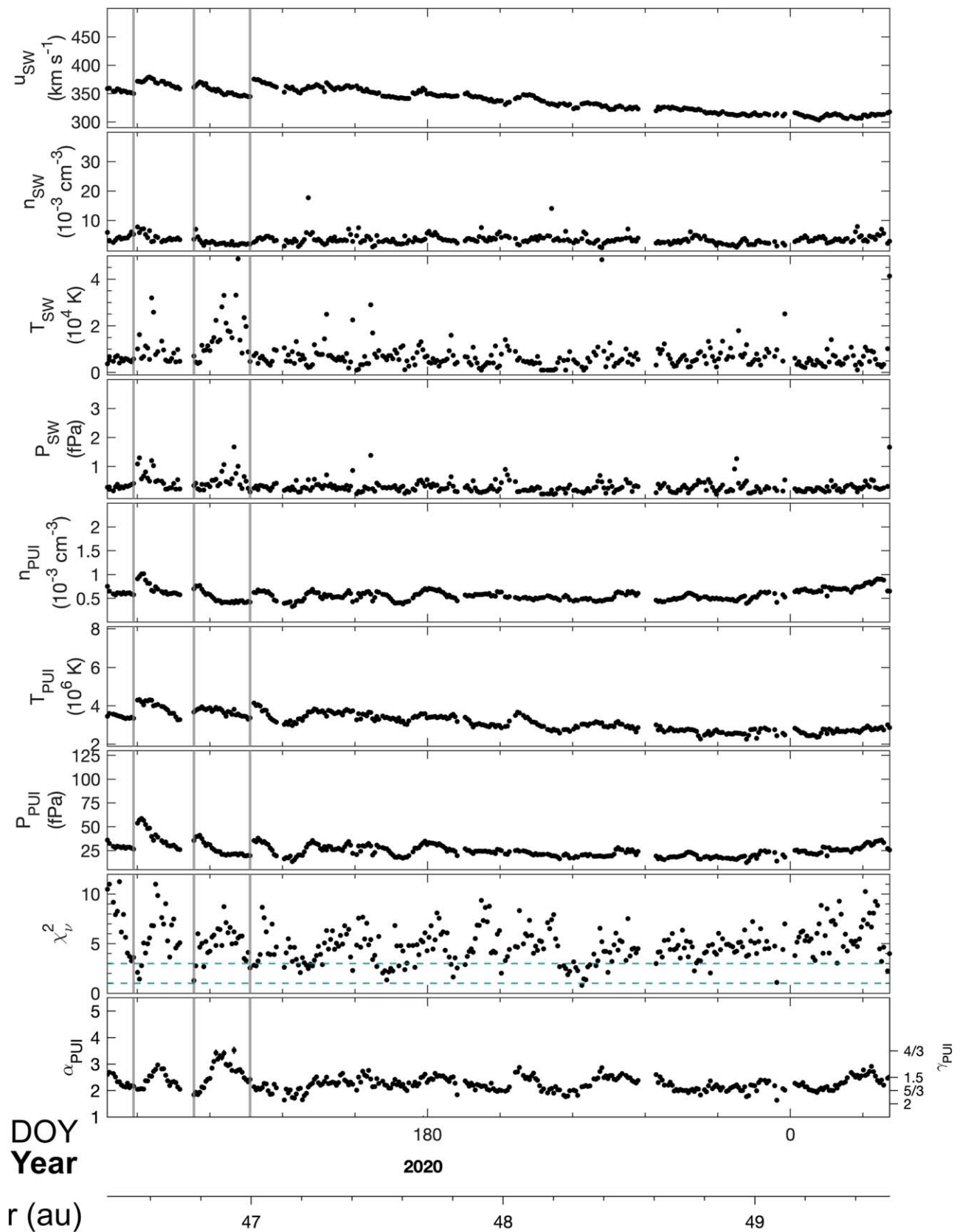


**Figure 1.** First publication of SWAP observation from the last interval of low time resolution SWAP data ( $\sim 46.4\text{--}49.5$  au). From top to bottom, the panels show the solar wind speed (which we also take as the bulk speed of the PUIs); solar wind density, temperature, and pressure; PUI density, temperature, and pressure; reduced  $\chi^2$  values ( $\chi^2_\nu$ ) of the fitting procedure; and the cooling index  $\alpha$ , or equivalently the PUI polytropic index  $\gamma$  (see text). Reduced  $\chi^2$  values of 1 (ideal) and 3 (very good) indicating the fitting, based on our experience with these data, are shown as horizontal dashed lines.

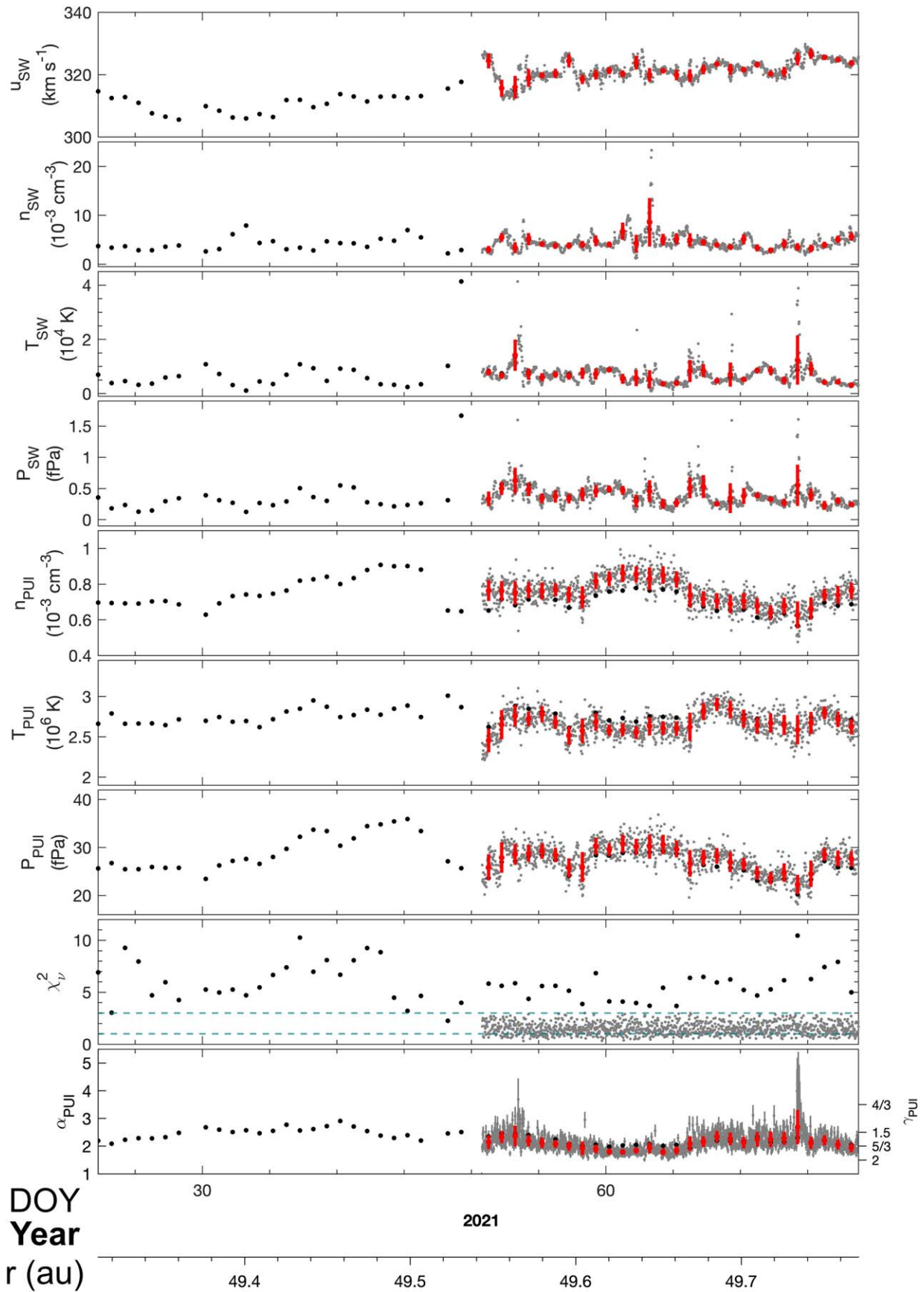


**Figure 2.** Data in the same format as Figure 1 for one solar rotation on either side of the transition from low to high time resolution data on 2021 February 19, when NH was at  $\sim 49.5$  au. The data shown are high-resolution (gray dots), day-long low-resolution (black dots), and day-averaged values and their standard deviations from the high-resolution data (red dots and bars). While the detailed analysis differs slightly for the low- and high-resolution observations, the results clearly provide a continuous data set that can be analyzed in a unified way.

different resolutions. In fact, we find it comforting that the reduced  $\chi^2$  values found for the day-interval points summed on the ground are so similar to those for the earlier data that were summed in space (typically  $\sim 3$ – $10$ ). We note that the reduced  $\chi^2$  reported here is the one that is minimized by our fitting procedure on a point-by-point basis to produce the moment-like PUI parameters. In general, lower values are better than higher ones, and the fitting of the high-resolution data is generally more accurate than for the low-resolution data, so the results should be considered superior. This is not surprising, as the solar wind has real variability over day-long intervals, and deriving moment-like parameters based on counts summed over such long intervals naturally leads to poorer values compared to statistically averaging groups of higher-resolution data. This allows us to cull any high-resolution data with reduced  $\chi^2$  values  $>3$ , as described above, which account for only 3.5% of the data points. Finally, we note that the reduced  $\chi^2$  should not be used in an absolute sense for comparison between individual data points because its property, the characterization of the goodness of fitting, is accurate only for linearly parameterized fit models; (error analysis of nonlinear parameterized fits, as done here, has additional terms not included in the chi-square formalism, e.g., G. Livadiotis 2007).

Thus, with Figure 2 and our new analyses in this study, we show that the combined observational data sets of low- and high-resolution data can be used together as a single data set. This is critical in order for both us and the broader community to be able to use the full, combined 22–60 au SWAP data set with high confidence, independent of whether the data were taken inside  $\sim 49.5$  au with low resolution or outside with high resolution.

The other interval of new observations that we examine for the first time in this study extends the high ( $\sim 30$  minute) time resolution PUI data from the end of the D. J. McComas et al. (2022) study on 2021 December 24, through our latest data on 2024 September 13 ( $\sim 52.0$ – $59.8$  au). Figure 3 shows this interval of new observations, which spans nearly three years in time and 8 au in heliocentric distance.

Overall, Figure 3 shows that the solar wind and PUI properties are highly structured on multiple temporal/spatial scales. On a larger scale, the solar wind speed is generally higher in 2023 than in 2022 or 2024, with typical values  $\sim 400$  km s $^{-1}$  as opposed to  $\sim 350$  km s $^{-1}$ , respectively. We commonly see the solar wind temperature and especially the PUI temperature rise for times of elevated solar wind speed. This correlation likely arises from several factors, including that fast solar wind is associated with higher temperatures than slow solar wind, faster solar wind produces higher local injection speeds for the PUIs, and the dominant energy in the solar wind—the flow energy ( $\rho v^2/2$ )—is greater for fast solar wind, so more energy is available to convert from the bulk flow into thermal PUI energy through solar wind compressions.

The new observations shown in Figure 3 also contain 14 new shocks (numbered 8–21), where we have  $\sim 30$  minute data; we identify these shocks by eye solely by looking for sharp changes in the solar wind speed on significantly time-expanded data plots, and while they all would likely have been detected in the old, lower time resolution data, the information about them is much greater with high time resolution. Table 1 provides a list of all 21 shocks observed so far with the high time resolution PUI data. These include the original seven examined by D. J. McComas et al. (2021) and these additional

14. B. L. Shrestha et al. (2024, in preparation) use the SWAP high-resolution data and this complete shock list to examine the properties of these 21 PUI-mediated shocks in detail.

### 3. Radial Variations in PUI Parameters

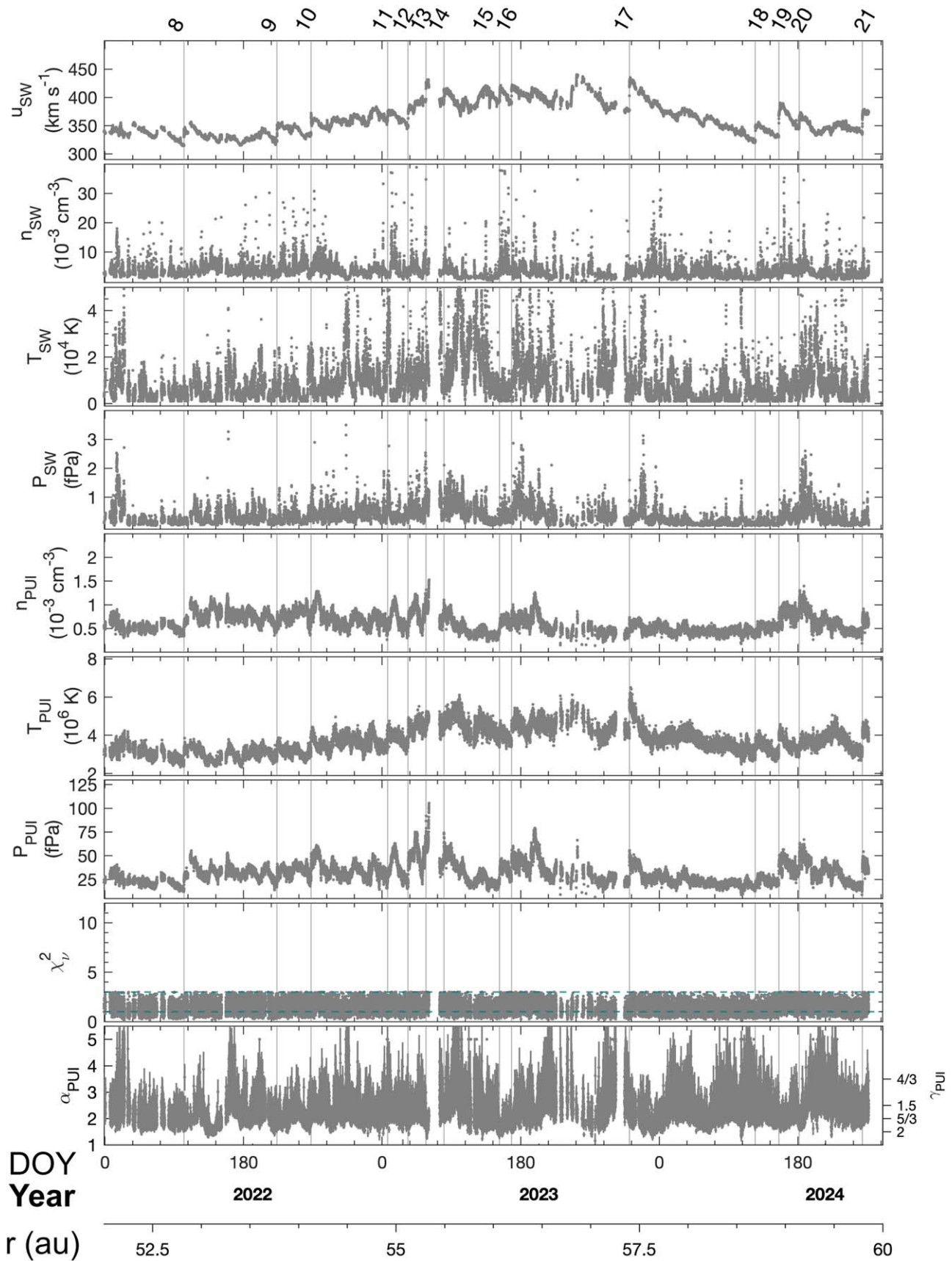
In this section, we use the new observations in our combined data set to examine the radial variations observed by SWAP from  $\sim 22$  to  $\sim 60$  au; the inner portions of these data were analyzed previously from  $\sim 22$  au out to  $\sim 38$  au by D. J. McComas et al. (2017) and then to 46.6 au by D. J. McComas et al. (2021). Now, with data out to  $\sim 60$  au, and more than a solar cycle of observations (2012 January 28–2024 September 13), the radial trends and shorter extrapolations to termination shock distances significantly improve our knowledge about how the PUIs evolve with distance and the conditions that we expect just ahead of the termination shock.

Figure 4 shows our nearly continuous PUI observations from  $\sim 22$  au through  $\sim 60$  au. These include the individual  $\sim 30$  minute high-resolution measurements (gray) starting on 2021 February 19, along with daily averaged measurements (black) before that date. We also averaged both the daily and high-resolution data separately into solar rotation (27.3 day) averaged points, which helps remove the sampling bias driven by different types of solar wind being emitted from different solar longitudes. These solar rotation points are shown as green dots with green vertical bars that indicate the  $\pm 1\sigma$  variability over each solar rotation.

The red solid lines in Figure 4 show power-law fits of the radial profiles using the solar rotation averaged data points. Because the solar wind variability over a solar rotation exceeds the instrumental uncertainties, the time variations of the parameters are not a measure of data uncertainty. Instead, because the variability in average values comes from real variations in the solar wind rather than observational uncertainties, we use unweighted fits that treat the values from each solar rotation equally in carrying out the power-law fits. Finally, we note that, while we use a nonlinear fitting here, just as we did in D. J. McComas et al. (2021), we also tried linear fitting and found that the results of the two were very close for all parameters (see below).

In this study, we find that the PUI density, temperature, and thermal pressure all drop off with heliocentric distance; their radial gradients are  $r^{-0.48}$ ,  $r^{-0.15}$ , and  $r^{-0.58}$ , respectively. The radial trend in the PUI temperature is significantly different than in our prior (D. J. McComas et al. 2021) study, which found an increasing PUI temperature with distance ( $r^{+0.18}$ ). We noted that a positive radial gradient was a concern in that study, as we do not expect the PUI heating to be so strong that it can fully overcome all the cooling from the expansion of the solar wind. The prior, erroneous gradient in PUI temperature was almost certainly due to a higher solar wind speed earlier in the solar cycle, which directly couples into this temperature. Further, the new, decreasing radial gradient in PUI temperature is more in line with general theoretical expectations.

The cooling parameter  $\alpha$  increases with a radial gradient of  $r^{+0.27}$ , or conversely, the polytropic index  $\gamma$  drops off as  $r^{-0.15}$ . This indicates that the PUI population is not only partially heating the expanding solar wind but is also heated itself from sources that can heat both populations, such as the dissipation of turbulent fluctuations (e.g., P. A. Isenberg et al. 2023).



**Figure 3.** Observations for the new extension of high time resolution data from SWAP (gray dots), in the same panel format as Figures 1 and 2. The 8th through 21st traveling interplanetary shocks identified in our high-resolution SWAP data are numbered and indicated by vertical lines.



**Table 1**  
Dates, Times, and Radial Distances of the 21 Shocks Sampled with High-resolution Data

Shock	Date	Time (UTC)	Radial Distance (au)
1	2021-03-22	04:58:42	49.79
2	2021-06-08	09:22:11	50.41
3	2021-08-31	04:58:43	51.08
4	2021-09-09	02:48:35	51.15
5	2021-10-07	20:52:19	51.38
6	2021-11-09	00:38:27	51.64
7	2021-12-05	12:34:11	51.85
8	2022-04-07	15:52:35	52.83
9	2022-08-06	13:39:15	53.78
10	2022-09-19	18:08:03	54.13
11	2022-12-28	04:58:43	54.92
12	2023-01-23	21:57:23	55.13
13	2023-02-16	00:38:27	55.32
14	2023-03-11	08:13:55	55.50
15	2023-05-22	17:44:35	56.07
16	2023-06-07	02:48:35	56.19
17	2023-11-07	04:24:35	57.40
18	2024-04-19	00:38:28	58.69
19	2024-05-19	14:47:32	58.93
20	2024-06-15	06:34:44	59.14
21	2024-09-05	09:49:56	59.79

Figure 5 shows the radial trends with distance in the ratios of various PUI properties and their respective core solar wind properties and/or ratios to total summed (PUI plus solar wind) values. As in our most recent study of the radial variations (D. J. McComas et al. 2021), we take the ratios of the parameters on a point-by-point basis (black for low-resolution data and gray for high-resolution data), which helps reduce the effect of solar wind density/pressure variations. For both cadences, we make solar rotation (27.3 day) averaged data points (green), again with vertical bars indicating the  $\pm 1\sigma$  standard deviation over each solar rotation. We then fit power-law functions to these averages. Again, we use nonlinear fits, but this time include the statistical weighting of the points, as we did in D. J. McComas et al. (2021), because the ratios of the parameters already take out some of the solar wind variability (see below for more discussion on fitting).

#### 4. Discussion

In this study, we add two new and significant segments of SWAP PUI observations: the final low-resolution (1 day) data from 2020 January 28 ( $\sim 46.4$  au) to 2021 February 18 ( $\sim 49.5$  au) and the most recent high-resolution ( $\sim 30$  minute) data from on 2021 December 24 ( $\sim 52.0$  au) through 2024 September 13 ( $\sim 59.8$  au). Together, these add almost 11 au of additional radial distance coverage and extend our nearly contiguous set of PUI observation from  $\sim 22$  to  $\sim 60$  au. The complete data set now spans almost 13 yr of observations, covering more than a full solar cycle. This is important because of the high variability of the solar wind conditions over the solar cycle, which previously made it hard to generate accurate radial trends with just the shorter intervals of data.

Table 2 summarizes the power-law radial dependencies and the standard errors and deviations of the PUI parameters from Figure 4, as well as the parameter ratios from Figure 5. In this table, we also provide the values of these fits at 60 au and

extrapolate them to a “nominal” termination shock distance of  $\sim 90$  au broadly across the upstream direction. This distance is simply a round number between the Voyager 1 termination shock crossing at  $\sim 94$  au (E. Stone et al. 2005) and Voyager 2 crossing at  $\sim 84$  au (E. Stone et al. 2008). The NH trajectory lies approximately in the ecliptic along the same heliographic longitude as Voyager 2. However, the location of the termination shock is variable over time (McComas et al. 2018b) as well as asymmetric about and offset (mostly northward) from the upwind direction (J. Richardson et al. 2008; D. J. McComas & N. A. Schwadron 2014; D. J. McComas et al. 2019; E. J. Zirnstein et al. 2022b), so it is uncertain at what distance NH may encounter it. Although the standard errors on these fits are small due to the high accuracy of the SWAP measurements, the standard deviations (in parentheses) are larger due to the natural time variability of the solar wind parameters. Therefore, the range of values extrapolated to all distances remains large, and actual values will depend on the solar wind conditions when NH reaches the termination shock.

For the results shown in Table 2 and throughout this study, the power-law profiles are derived from a nonlinear fitting. For each variable  $x$ , this is expressed by  $x(r) = x_{60} \cdot (r/60)^A$  (with the heliospheric distance  $r$  in au), which involves the two fitting parameters of the radial exponent  $A$  and the  $x$ -value at 60 au. The power-law constant was chosen to correspond to  $r = 60$  au in order to minimize the propagation error of the extrapolation to 90 au, and the corresponding 90 au value,  $x_{90} = x_{60} \cdot 1.5^A$ , is propagated with error  $\delta \ln x_{90} = \sqrt{(\delta \ln x_{60})^2 + 0.16 \delta A^2}$  (where  $\delta \ln x = \delta x/x$ ). We tested four different methods of fitting and compared their accuracy; these were combinations of weighted/unweighted and linear/nonlinear fitting procedures. We determined that the best precision of derived parameters (and thus, the highest goodness of fitting) was derived from the unweighted nonlinear fits for the PUI parameters and the weighted nonlinear fits for their ratios with the respective solar wind parameters. The derived statistics are shown in Table 2 in standard notation of  $\bar{x} \pm \delta x (\sigma_x)$ , where the fitted optimal value of the parameter  $\bar{x}$  is given with its standard error  $\delta x$ , a measure of the precision of the fitted value  $\bar{x}$ , and its standard deviation  $\sigma_x$ , a measure of the variability of the analyzed  $x$ -values. We have used  $\delta x = \sigma_x/\sqrt{N}$ , where  $N = 165$  is the number of data bins averaged over a Carrington rotation used for fitting the power-law profiles.

We find that, by 60 au, the average PUI thermal pressure is  $\sim 11\%$  that of the solar wind dynamic pressure, and it has reached  $\sim 21\%$  by 90 au. Such large values emphasize how important PUIs are in the physics of the termination shock. We also show that, by 60 au, nearly a fifth ( $\sim 18\%$ ) of the total protons are PUIs ( $n_{\text{PUI}}/n_{\text{Total}}$ ), and are not from the original, core solar wind. Around a termination shock distance of 90 au, that average value could climb to  $\sim 30\%$ . The derived radial exponent of 1.19 is only slightly larger than linear, which is consistent with theoretical expectations of a roughly linear increase in this ratio (e.g., M. A. Lee et al. 2009). In addition, PUIs representing 30% of the  $\text{H}^+$  ions at the termination shock are consistent with global heliospheric models (Malama et al. 2006; E. J. Zirnstein et al. 2017; J. Heerikhuisen et al. 2019) that predicted ratios of  $\sim 20\%$ – $25\%$  near the upstream termination shock, based on values of the ISN H density that were lower than those more recently determined from SWAP observations (P. Swaczyna et al. 2020).



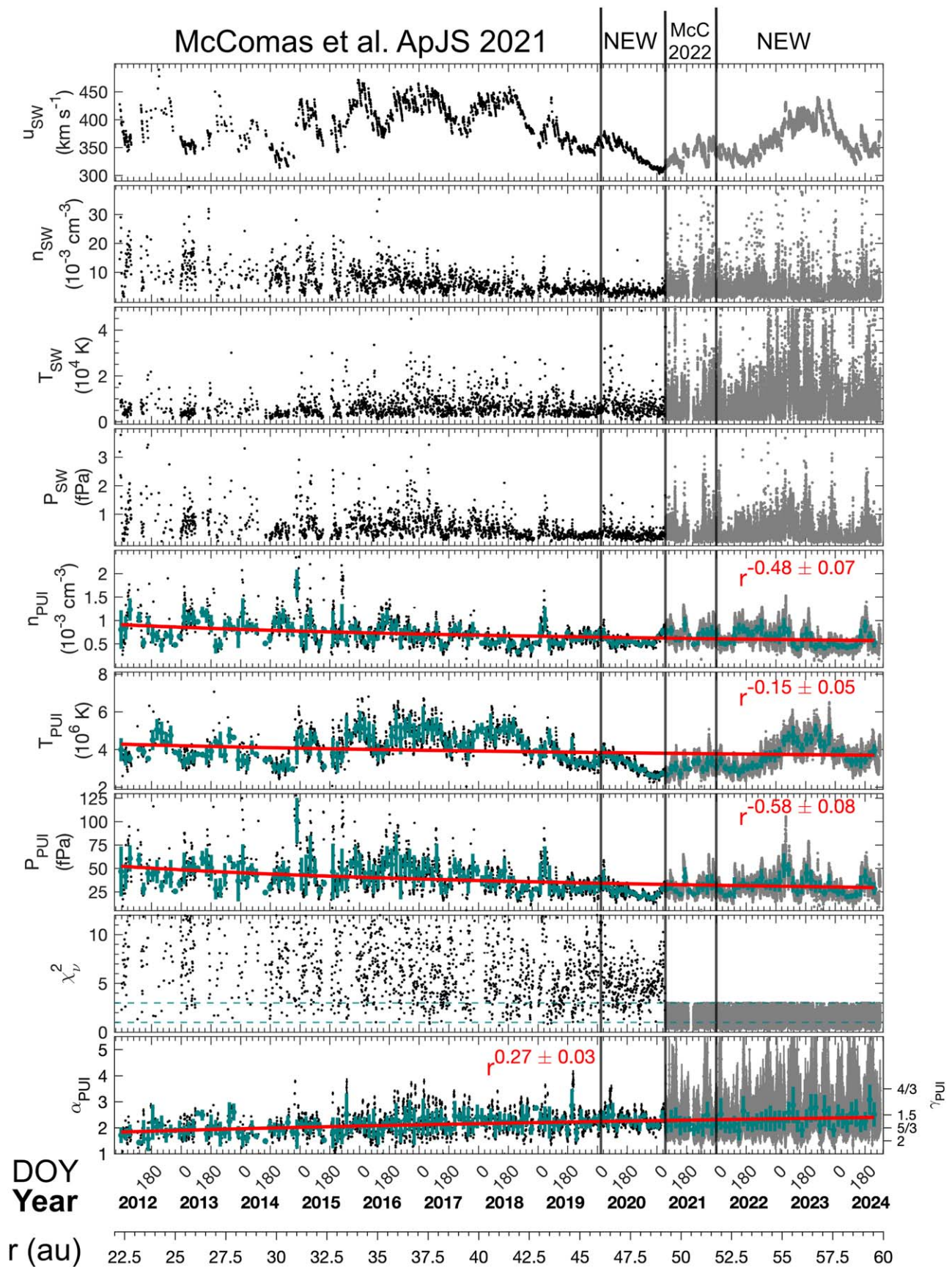


**Figure 4.** Plot of complete SWAP data set from 22 to 60 au, spanning from 2012 through most of 2024. Vertical lines and labels at the top indicate previously published data vs. those that are newly analyzed in this study. Gray dots show high-resolution ( $\sim 30$  minute) data, while black dots give day-averaged values. Green points show further averaging over full solar rotations (27.3 days), and red lines show the power-law fits to those rotation-averaged values.

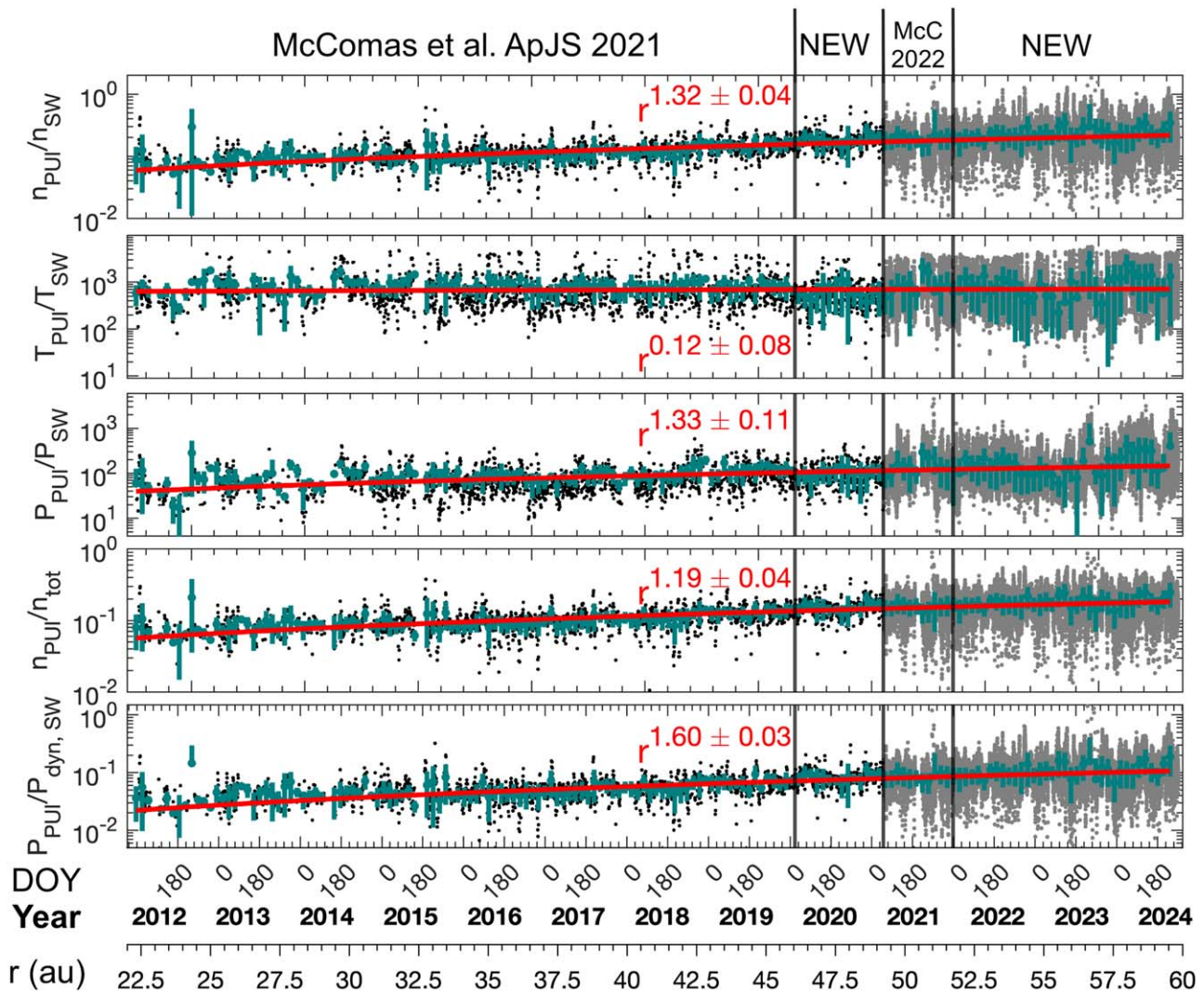


**Figure 5.** Ratios of PUI parameters taken for individual daily or  $\sim 30$  minute measurements and then processed and plotted as in Figure 4. The panels show, from top to bottom, the ratios of the PUI to the solar wind (SW) density, temperature, and thermal pressure; the ratio of the PUI to the total (Tot, summed PUI and SW) density; and the ratio of the PUI to the solar wind dynamic pressure (dyn,  $\rho v^2/2$ ).

The polytropic index  $\gamma$  of the PUIs is  $\sim 1.5$  at 60 au, and a slowly decreasing radial gradient  $\sim -0.23/r$  [au] reveals that the PUI population is heated and will continue to be heated farther out in the heliosphere. The origin of PUI heating can be caused via multiple mechanisms. PUIs are stochastically accelerated in both the pre-existing and self-generated magnetic field turbulence (e.g., T. J. Bogdan et al. 1991; le Roux & Ptuskin 1998; P. A. Isenberg 2005; S. V. Chalov et al. 2006; H. J. Fahr & H. Fichtner 2011; K. V. Gamayunov et al. 2012; P. A. Isenberg et al. 2023). P. Mostafavi et al. (2017, 2018) theoretically reproduced relatively cold thermal plasma with preferential PUI heating at PUI-mediated traveling interplanetary shocks, showing the importance of energetic particles in the shock structure for most magnetic field orientations. Using particle-in-cell simulations, R. Kumar et al. (2018) showed that adiabatic compression of the solar wind ahead of a shock could also heat the PUIs. In parallel, G. P. Zank et al. (2018) developed a general theoretical framework, including PUIs, solar wind, IMF, and low-frequency turbulence, and showed how PUIs both interact with the pre-existing low-frequency turbulence and further enhance scattering of the PUIs and heating of thermal ions. These authors were able to generally

reproduce SWAP’s observed non-adiabatic solar wind temperature profile.

With the introduction of the first radial trends of interstellar PUI moments beyond 20 au from the Sun (D. J. McComas et al. 2017), theoreticians and modelers have worked hard to reproduce the observations in several ways. For example, analytical models of the solar wind mediated by PUIs in the presence of turbulence compared reasonably well to the observed PUI moments out to  $\sim 38$  au (G. P. Zank et al. 2018) and  $\sim 50$  au (L. Adhikari et al. 2023) from the Sun. A test particle model showed that spatial diffusion enhances the effects of cooling by adiabatic expansion close to the Sun but becomes unimportant beyond  $\sim 15$  au, where PUIs dominate the thermal pressure of the bulk solar wind mixture (L.-L. Zhao et al. 2019). Most models like these, however, are in a steady state with constant and uniform boundary conditions.

More sophisticated, time-dependent MHD models of the heliosphere have shown reasonable agreement with the evolution of SWAP observations of PUIs over time. For example, the 1 au OMNI data-driven model by T. Kim et al. (2018) and their model extended further in time by F. Fraternali et al. (2022) compare quite well to the observed PUI



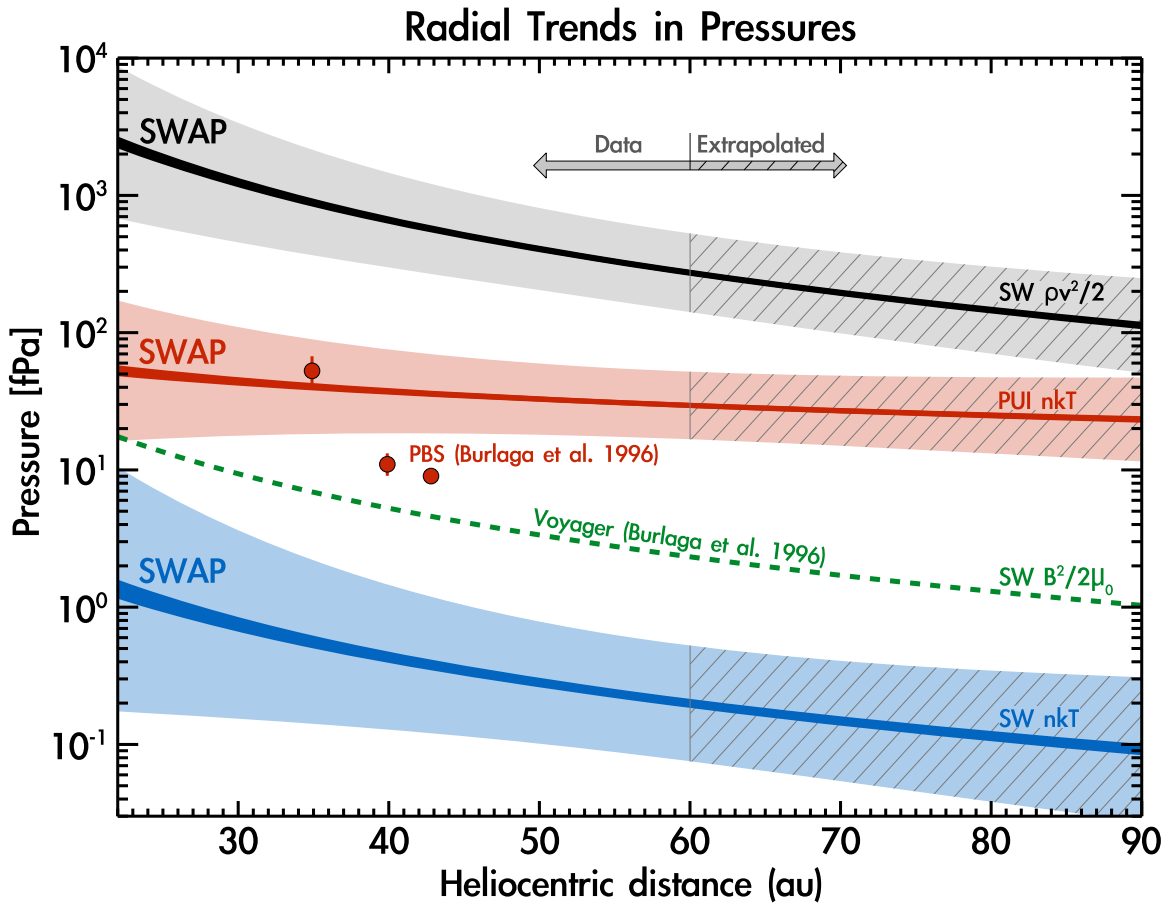


**Figure 6.** Fits to the solar wind and PUI observations from SWAP, including standard errors (thicker lines) and standard deviations (shading). SWAP data were nearly continuously collected from  $\sim 22$  to 60 au, with extrapolated values beyond that (cross-hatched). SWAP data are used for the solar wind dynamic pressure (black), PUI pressure (red), and solar wind thermal pressure (blue). We also plot the magnetic pressure (green dashed line) and three pressure balance structures (PBSs; red dots) from much earlier Voyager data (L. F. Burlaga et al. 1996).

**Table 2**  
Power-law Fit Exponents and Values at 60 au and Extrapolated to 90 au, in the Format: Value  $\pm$  Standard Error (Standard Deviation)

Variables ( $x$ )	Value at 60 au		Extrapolated to 90 au
	Exponent ( $A$ )	$x_{60}$	$x_{90}$
$n_{\text{PUI}}$	$-0.48 \pm 0.07$ (0.91)	$5.68 \pm 0.22$ ( $2.86$ ) $\times 10^{-4}$ $\text{cm}^{-3}$	$4.69 \pm 0.23$ ( $2.92$ ) $\times 10^{-4}$ $\text{cm}^{-3}$
$T_{\text{PUI}}$	$-0.15 \pm 0.05$ (0.66)	$3.69 \pm 0.10$ ( $1.22$ ) $\times 10^6$ K	$3.48 \pm 0.12$ ( $1.48$ ) $\times 10^6$ K
$P_{\text{PUI}}$	$-0.58 \pm 0.08$ (0.98)	$29.5 \pm 1.3$ (16.3) fPa	$23.3 \pm 1.2$ (15.8) fPa
$\alpha_{\text{PUI}}$	$0.27 \pm 0.03$ (0.41)	$2.40 \pm 0.03$ (0.44)	$2.68 \pm 0.05$ (0.67)
$\gamma_{\text{PUI}}$	$-0.150 \pm 0.016$ (0.208)	$1.525 \pm 0.013$ (0.161)	$1.435 \pm 0.015$ (0.194)
$\frac{n_{\text{PUI}}}{n_{\text{SW}}}$	$1.32 \pm 0.04$ (0.56)	$0.220 \pm 0.006$ (0.075)	$0.376 \pm 0.012$ (0.155)
$\frac{T_{\text{PUI}}}{T_{\text{SW}}}$	$0.12 \pm 0.08$ (1.06)	$720 \pm 50$ (610)	$750 \pm 60$ (710)
$\frac{P_{\text{PUI}}}{P_{\text{SW}}}$	$1.33 \pm 0.11$ (1.36)	$148 \pm 9$ (114)	$253 \pm 19$ (240)
$\frac{n_{\text{PUI}}}{n_{\text{total}}}$	$1.19 \pm 0.04$ (0.48)	$0.184 \pm 0.004$ (0.052)	$0.298 \pm 0.008$ (0.102)
$\frac{P_{\text{PUI}}}{P_{\text{SW-Dyn}}}$	$1.60 \pm 0.03$ (0.45)	$0.108 \pm 0.003$ (0.037)	$0.206 \pm 0.006$ (0.081)

moments at time scales on the order of a Carrington rotation. Other time-dependent models that use more idealized solar cycle boundary conditions also compare well to the data, although not in reproducing the small-timescale variability, where PUIs are treated as a separate fluid in the models (R. K. Bera et al. 2023; F. Fraternali et al. 2024).

Finally, the cooling index previously used to describe the heating/cooling of PUIs measured by SWAP was shown to be directly related to the kappa index of kappa distributions that

describe space plasmas (G. Livadiotis et al. 2024). By making this connection, G. Livadiotis et al. (2024) showed good agreement between independent predictions of the kappa index as a function of distance from the Sun with SWAP PUI observations, as well as agreement over large radial distances, between measurements taken at 1 au from Wind,  $\sim 50$  au from SWAP, and  $\sim 100$  au from remote observations by IBEX.

Figure 6 compiles the radial variations of the SWAP pressure observations from  $\sim 22$  to 60 au, and extrapolated values from



60 to 90 au. The solar wind dynamic pressure is shown in black. We calculate this from  $P_{\text{PUI}}/(P_{\text{PUI}}/P_{\text{SW-Dyn}})$ , where the numerator and denominator are from the fits in Table 2. Similarly, the solar wind thermal pressure (blue) is calculated via  $P_{\text{PUI}}/(P_{\text{PUI}}/P_{\text{SW}})$ . SWAP average values, including their standard errors, are indicated by the dark colored lines and their thicknesses, respectively, while the standard deviations from the large variability of the physical parameters are indicated by the surrounding light-colored shading. Typical solar wind plasma moments have values whose fluctuations follow the statistics of a lognormal distribution (e.g., L. F. Burlaga & A. J. Lazarus 2000). The standard deviation of the logarithm of a parameter,  $x = x_{60} \cdot (r/60)^A$ , is  $\sigma_{\ln x} = \sqrt{\sigma_{\ln x_{60}}^2 + \ln^2(r/60) \cdot \delta\sigma_A^2}$ , and the corresponding plot shows  $1\sigma$  fluctuation according to  $e^{\ln x \pm \sigma_{\ln x}} = x \cdot e^{\pm \sigma_{\ln x}}$ . Extrapolated values are indicated by cross-hatching. We also include three early estimates of the PUI pressure made by L. F. Burlaga et al. (1996) using the presence of pressure balance structures in the solar wind, and the magnetic pressure from Voyager observations (dashed green line). Comparison with the much earlier Voyager magnetic field data is required because NH does not carry a magnetometer and thus makes no direct observations of the IMF.

As shown in our earlier studies (D. J. McComas et al. 2017, 2021) and extended in Figure 6 with the new radial gradients found here, the PUI thermal pressure is already dominant over the solar wind thermal pressure and magnetic field pressure well inside of 20 au and continues to grow with increasing radial distance. By 60 au the average PUI pressure is over an order of magnitude larger than the magnetic field pressure and over 2 orders of magnitude greater than the core solar wind thermal pressure. From 60 to 90 au, our data indicate that, on average, this dominance just continues to grow.

The continuously increasing percentage of total pressure that is held by PUI thermal pressure can also be understood from a simple thermodynamic perspective. Solar wind protons are thermalized, residing in stationary states (thermal equilibrium) described by kappa distributions for which the entropy has evolved and stabilized at its maximum value, determined as a function of the thermodynamic parameters (temperature and kappa). Any change of the entropy can only lead to a respective change of the involved thermodynamic parameters (e.g., see G. Livadiotis & D. J. McComas 2023). Thus, all space plasma processes affecting the solar wind thermal pressure are subject to the laws of thermodynamic equilibrium. On the other hand, PUIs are neither thermalized, nor residing in stationary states. The respective thermodynamic parameters can be approached through “equivalence” definitions, e.g., an equivalent definition of temperature allows the usage of the mean kinetic energy (e.g., G. P. Zank et al. 2010). Since their distribution is not thermalized, it is subject to changes caused by either thermal or nonthermal mechanisms (i.e., not restricted to changes allowed by the laws of thermodynamic equilibrium). Both thermal and nonthermal PUI energization leads to an increase of equivalent temperature and thermal pressure.

Extrapolation of SWAP PUI radial profiles provides the only direct observational data about the likely conditions, just upstream of the termination shock. We find that, by 60 au, the PUI pressure is already  $\sim 11\%$  of the solar wind ram pressure that carries the vast majority of the solar wind energy flux out from the Sun. By 90 au, our extrapolations predict that this will nearly double, to over 20%. This study is the first time that we have fully included the variability (standard errors and standard

deviations) of the solar wind and PUI pressures. Interestingly, these show clearly how variable the solar wind and PUI pressures are in the outer heliosphere, and the PUI thermal and solar wind dynamic pressure standard deviations even touch near 90 au, suggesting that occasionally the PUI pressure could even be greater than the dynamic pressure in the outermost reaches of the solar wind. Of course, both the PUI thermal and solar wind dynamic pressures tend to be larger for greater solar wind speeds, so this inversion may not actually occur. The transition from supersonic to subsonic at the termination shock, or when the thermal pressure of the entire solar wind plus PUI mixture is greater than the dynamic pressure of the mixture, is most likely when the PUI thermal pressure will greatly exceed the dynamic flow energy of the plasma.

What we have learned from SWAP about the physics of PUI-mediated, traveling interplanetary shocks (D. J. McComas et al. 2017, 2021, 2022; E. J. Zirnstein et al. 2018; B. L. Shrestha et al. 2024) is also critical for understanding the termination shock, which must also be strongly mediated by PUIs (e.g., G. P. Zank et al. 1996, 2010; R. B. Decker et al. 2008). This mediation explains why the Voyager 2 plasma observations did not show significant heating of the core solar wind plasma at the termination shock crossing (J. Richardson et al. 2008). This is because PUIs have higher thermal energies and thus act as seed particles for shock acceleration (e.g., L. A. Fisk & M. A. Lee 1980, N. A. Schwadron et al. 1996, S. V. Chalov 2001, J. Giacalone et al. 2002, L. A. Fisk & G. Gloeckler 2006, 2007, 2008; J. H. Chen et al. 2015; E. J. Zirnstein et al. 2021), due to their preferential heating at quasi-perpendicular shocks (e.g., G. P. Zank et al. 2010).

SWAP will continue to make high-resolution observations of the solar wind and interstellar H PUI populations as NH continues to transit outward toward the termination shock at nearly 3 au per year. Given that only Voyager 1 and 2 have crossed the termination shock, the solar wind variability, and the asymmetric shape, any prediction of when NH will cross is attached with large range of uncertainty. Additionally, solar wind pressure changes have been estimated to alter the termination shock location by more than 10 au (H. Washimi et al. 2011), further adding to the uncertainty. If and when NH finally crosses the termination shock, SWAP’s first-ever PUI observations across the termination shock will be truly fundamental to understanding the structure and physical processes of the shock, including the critical energy partitioning at the termination shock, which the Voyager measurements could not address (R. B. Decker et al. 2008). In the meantime, SWAP’s unique observations will continue to be critical for understanding the outer heliosphere and PUI dominated plasmas more generally.

In parallel, NASA’s Interstellar Mapping and Acceleration Probe (IMAP) mission (McComas et al. 2018a) will launch in 2025. IMAP will explore particle acceleration directly in the solar wind and through remote ENA imaging and sampling of interstellar neutral atoms and dust that survive into 1 au. These combined and synergistic observations will substantially improve our understanding of the outer heliosphere, the VLISM, and the interaction between the two.











This paper serves as the citable reference for the complete SWAP PUI observations from  $\sim 22$  to 60 au. These data are available through the Space Physics at Princeton website (<https://spacephysics.princeton.edu/missions-instruments/swap/pui-data-2025>) and will be submitted to the NASA SPDF repository. Both

the SWAP low- and high-resolution data and processing are complicated, and the derived PUI parameters should be used with caution. While we strongly encourage the broader scientific community to use SWAP data for your own research, we also encourage you to reach out to the SWAP instrument PI, D. J. McComas, at [dmccomas-at-princeton.edu](mailto:dmccomas-at-princeton.edu), and work with the SWAP team when using these data.

### Acknowledgments

We gratefully thank all the SWAP instrument and NH mission team members. This work was carried out as a part of the SWAP instrument effort on the NH project (M99023MJM; PU-AWD1006357), with support from NASA's New Frontiers Program and the IMAP mission, as a part of NASA's Solar Terrestrial Probes (STP) mission line (80GSFC19C0027).

### ORCID iDs

D. J. McComas  <https://orcid.org/0000-0001-6160-1158>  
 B. L. Shrestha  <https://orcid.org/0000-0002-5247-4107>  
 G. Livadiotis  <https://orcid.org/0000-0002-7655-6019>  
 J. R. Szalay  <https://orcid.org/0000-0003-2685-9801>  
 E. J. Zirnstein  <https://orcid.org/0000-0001-7240-0618>  
 H. A. Elliott  <https://orcid.org/0000-0003-2297-3922>  
 P. C. Brandt  <https://orcid.org/0000-0002-4644-0306>  
 A. R. Poppe  <https://orcid.org/0000-0001-8137-8176>  
 K. N. Singer  <https://orcid.org/0000-0003-3045-8445>  
 A. Stern  <https://orcid.org/0000-0001-5018-7537>  
 A. Verbiscer  <https://orcid.org/0000-0002-3323-9304>

### References

- Adhikari, L., Zank, G. P., Wang, B., et al. 2023, *ApJ*, **953**, 44  
 Bera, R. K., Fraternali, F., Pogorelov, N. V., et al. 2023, *ApJ*, **954**, 147  
 Bogdan, T. J., Lee, M. A., & Schneider, P. 1991, *JGR*, **96**, 161  
 Burlaga, L. F., & Lazarus, A. J. 2000, *JGR*, **105**, 2357  
 Burlaga, L. F., Ness, N. F., Belcher, J. W., et al. 1996, *SSRv*, **78**, 33  
 Chalov, S. V. 2001, *JGR*, **106**, 18667  
 Chalov, S. V., Alexashov, D. B., & Fahr, H. J. 2006, *ASTRA*, **2**, 19  
 Chen, J. H., Bochsler, P., Möbius, E., & Gloeckler, G. 2014, *JGRA*, **119**, 7142  
 Chen, J. H., Schwadron, N. A., Möbius, E., & Gorby 2015, *JGRA*, **120**, 9269  
 Decker, R. B., Krimigis, S. M., Roelof, E. C., et al. 2008, *Natur*, **454**, 67  
 Elliott, H. A., McComas, D. J., Valek, P., et al. 2016, *ApJS*, **223**, 19  
 Elliott, H. A., McComas, D. J., Zirnstein, E. J., et al. 2019, *ApJ*, **885**, 156  
 Elliott, H. A., Valek, P., McComas, D. J., et al. 2018, *ApJ*, **866**, 85  
 Fahr, H. J., & Fichtner, H. 1995, *SoPh*, **158**, 353  
 Fahr, H. J., & Fichtner, H. 2011, *A&A*, **533**, A92  
 Fahr, H. J., & Scherer, K. 2005, *JGR*, **110**, A02103  
 Fisk, L. A., & Gloeckler, G. 2006, *ApJL*, **640**, L79  
 Fisk, L. A., & Gloeckler, G. 2007, *PNAS*, **104**, 5749  
 Fisk, L. A., & Gloeckler, G. 2008, *ApJ*, **686**, 1466  
 Fisk, L. A., & Lee, M. A. 1980, *ApJ*, **237**, 620  
 Fraternali, F., Adhikari, L., Fichtner, H., et al. 2022, *SSRv*, **218**, 50  
 Fraternali, F., Pogorelov, N. V., & Bera, R. K. 2024, *ApJL*, **974**, L15  
 Gamayunov, K. V., Zhang, M., Pogorelov, N., et al. 2012, *ApJ*, **757**, 74  
 Giacalone, J., Jokipii, J. R., & Kóta, J. 2002, *ApJ*, **573**, 845  
 Geiss, J., Gloeckler, G., Mall, U., et al. 1994, *A&A*, **282**, 924  
 Gloeckler, G., Fisk, L. A., & Geiss, J. 1997, *Natur*, **386**, 374  
 Gloeckler, G., Geiss, J., Balsiger, H., et al. 1992, *A&A*, **92**, 267  
 Heerikhuisen, J., Zirnstein, E. J., Pogorelov, N. V., Zank, G. P., & Desai, M. 2019, *ApJ*, **874**, 76  
 Intriligator, D. S., Siscoe, G. L., & Miller, W. D. 1996, *GeoRL*, **23**, 2128  
 Isenberg, P. A. 2005, *ApJ*, **623**, 502  
 Isenberg, P. A., Vasquez, B. J., & Smith, C. W. 2023, *ApJ*, **944**, 84  
 Kim, T. K., Pogorelov, N. V., & Burlaga, L. F. 2017, *ApJL*, **843**, L32  
 Kumar, R., Zirnstein, E. J., & Spitkovsky, A. 2018, *ApJ*, **860**, 156  
 Lee, M. A. 1999, *Ap&SS*, **264**, 497  
 Lee, M. A., Fahr, H. J., Kucharek, H., et al. 2009, *SSRv*, **146**, 275  
 Le Roux, J. A., & Puskin, V. S. 1998, *JGR*, **103**, 4799  
 Livadiotis, G. 2007, *PhysA*, **375**, 518  
 Livadiotis, G., & McComas, D. J. 2023, *ApJ*, **954**, 72  
 Livadiotis, G., McComas, D. J., & Shrestha, B. L. 2024, *ApJ*, **968**, 66  
 Malama, Y. G., Izmodenov, V. V., & Chalov, S. V. 2006, *A&A*, **445**, 693  
 McComas, D. J., Allegrini, F., Bagenal, F., et al. 2008, *SSRv*, **140**, 261  
 McComas, D. J., Bzowski, M., Fuselier, S. A., et al. 2015, *ApJS*, **220**, 22  
 McComas, D. J., Christian, E. R., Schwadron, N. A., et al. 2018a, *SSRv*, **214**, 116  
 McComas, D. J., Daych, M. A., Funsten, H. O., et al. 2018b, *ApJL*, **856**, L10  
 McComas, D. J., Elliott, H. A., & Schwadron, N. A. 2010, *JGR*, **115**, A03102  
 McComas, D. J., Rankin, J. S., Schwadron, N. A., et al. 2019, *ApJ*, **884**, 145  
 McComas, D. J., & Schwadron, N. A. 2014, *ApJL*, **795**, L17  
 McComas, D. J., Schwadron, N. A., Crary, F. J., et al. 2004, *JGR*, **109**, A02104  
 McComas, D. J., Shrestha, B. L., Swaczyna, P., et al. 2022, *ApJ*, **934**, 2  
 McComas, D. J., Swaczyna, P., Szalay, J. R., et al. 2021, *ApJS*, **254**, 19  
 McComas, D. J., Zirnstein, E. J., Bzowski, M., et al. 2017, *ApJS*, **233**, 8  
 Mihalov, J. D., & Gazis, P. R. 1998, *GeoRL*, **25**, 3 241  
 Möbius, E., Hovestadt, D., Klecker, B., et al. 1985, *Natur*, **318**, 426  
 Mostafavi, P., Zank, G. P., & Webb, G. M. 2017, *ApJ*, **841**, 4  
 Mostafavi, P., Zank, G. P., & Webb, G. M. 2018, *ApJ*, **868**, 120  
 Randol, B. M., Elliott, H. A., Gosling, J. T., McComas, D. J., & Schwadron, N. A. 2012, *ApJ*, **755**, 75  
 Randol, B. M., McComas, D. J., & Schwadron, N. A. 2013, *ApJ*, **768**, 120  
 Richardson, J., Kasper, J., Wang, C., et al. 2008, *Natur*, **454**, 63  
 Ruciński, D., & Bzowski, M. 1995, *A&A*, **296**, 248  
 Schwadron, N. A., Fisk, L. A., & Gloeckler, G. 1996, *GeoRL*, **23**, 2871  
 Shrestha, B. L., Zirnstein, E. J., McComas, D. J., et al. 2024, *ApJ*, **960**, 35  
 Sokol, J. M., Kubiak, M. A., & Bzowski, M. 2019, *ApJ*, **879**, 24  
 Stone, E., Cummings, A., McDonald, F., et al. 2005, *Sci*, **309**, 2017  
 Stone, E., Cummings, A., McDonald, F., et al. 2008, *Natur*, **454**, 71  
 Swaczyna, P., McComas, D. J., & Zirnstein, E. J. 2019, *ApJ*, **875**, 36  
 Swaczyna, P., McComas, D. J., Zirnstein, E. J., et al. 2020, *ApJ*, **903**, 48  
 Vasyliunas, V. M., & Siscoe, G. L. 1976, *JGR*, **81**, 1247  
 Washimi, H., Zank, G. P., Hu, Q., et al. 2011, *MNRAS*, **416**, 1475  
 Zank, G. P., Adhikari, L., Zhao, L.-L., et al. 2018, *ApJ*, **869**, 23  
 Zank, G. P., Heerikhuisen, J., Pogorelov, N. V., Burrows, R., & McComas, D. 2010, *ApJ*, **708**, 1092  
 Zank, G. P., Pauls, H. L., Cairns, I. H., & Webb, G. M. 1996, *JGR*, **101**, 457  
 Zhao, L.-L., Zank, G. P., & Adhikari, L. 2019, *ApJ*, **879**, 32  
 Zirnstein, E. J., Heerikhuisen, J., Zank, G. P., et al. 2017, *ApJ*, **836**, 238  
 Zirnstein, E. J., Kumar, R., Bandyopadhyay, R., et al. 2021, *ApJL*, **916**, L21  
 Zirnstein, E. J., McComas, D. J., Kumar, R., et al. 2018, *PhRvL*, **121**, 075102  
 Zirnstein, E. J., Möbius, E., Zhang, M., et al. 2022a, *SSRv*, **218**, 28  
 Zirnstein, E. J., Shrestha, B. L., McComas, D. J., et al. 2022b, *NatAs*, **6**, 1398